Constructing electron transport channel of $SnO_2/BaSO_4$ on g-C_3N_4 for enhanced visible-light-driven photocatalytic H_2 production

Gongyue Dong[a], Xiaojuan Guo[b], Cheng Cheng[a,*], Feng Chen[a,d], Jinfeng Zhang[a], Yanping Du[c,*], Wei Meng[e], Maochang Liu[a], Jinwen Shi[a,*]

[a] *International Research Center for Renewable Energy, State Key Laboratory of Multiphase Flow in Power Engineering, Xi'an Jiaotong University, Xi'an 710049, China*

[b] *Guangdong Provincial Key Laboratory of Multi-energy Complementary Distributed Energy Systems, Dongguan University of Technology, Dongguan 523808, China*

[c] *School of Engineering, Lancaster University, Lancaster LA1 4YW, UK*

[d] *Gansu Company, PipeChina, Lanzhou 730060, China*

[e] *Hunan Provincial Key Lab of Dark Tea and Jin-Hua, Department of Material & Chemical Engineering, Hunan City University, Yiyang 413000, China*

[*] Corresponding authors.

E-mail Address: ccheng-xjtu@xjtu.edu.cn (C. Cheng)
y.du17@lancaster.ac.uk (Y. Du)
jinwen_shi@mail.xjtu.edu.cn (J. Shi)

Abstract

Graphitic carbon nitride (g-C_3N_4) is confronted with the issue of poor utilization of photogenerated charge carriers, thereby leading to limited performance of photocatalytic hydrogen (H_2) production, which restricts its potential application. Herein, the electron transport material $SnO_2/BaSO_4$ was synthesized to integrate with g-C_3N_4 for addressing the above problem. Various characterizations were conducted to investigate the g-C_3N_4-$SnO_2/BaSO_4$ photocatalyst, and it demonstrated that photogenerated electrons from g-C_3N_4 expeditiously migrate to $SnO_2/BaSO_4$ nanoparticles, which markedly hindered photogenerated carriers' recombination. Subsequently, the g-C_3N_4-$SnO_2/BaSO_4$ photocatalyst demonstrated promoted photocatalytic H_2 production at a rate of 14.2 μmol h^{-1} under visible-light illumination, which was 2.5 times higher than that of pristine g-C_3N_4.

Keywords: Photocatalysis; Graphitic carbon nitride; Tin dioxide; Barium sulfate; Electron transport material.

1. Introduction

Developing clean and sustainable energy has been urgently required to mitigate the severe repercussions associated with the utilization of fossil fuels[1, 2]. A kind of energy that has been garnering increasing attention is hydrogen (H_2), owing to several advantages of high energy density, renewability, pollution-free combustion product, long-term storage capability, and flexibility in application [3-5]. Within the realm of H_2 production technology, photocatalytic H_2 production has emerged as an avenue with wide prospect to harness H_2 energy from abundant and renewable solar energy through water splitting [6, 7]. An imperative aspect of this process is developing efficient photocatalysts to enhance the performance of photocatalytic H_2 production [8, 9].

Recently, a significant number of researchers have gravitated towards graphitic carbon nitride (g-C_3N_4), following Wang group's groundbreaking study on its visible-light-driven photocatalytic H_2 production [10]. Noteworthy features of g-C_3N_4 involve its π-conjugated two-dimensional (2D) layered structure, a moderate bandgap (approximately 2.7 eV), and a range of superiorities including high thermal and chemical stability, nontoxicity, the composition of earth-abundant elements, and ease of preparation using cost-effective precursors, which collectively position g-C_3N_4 as a strong contender in photocatalysis [11-13]. Nevertheless, despite its merit, the photocatalytic activity of pristine g-C_3N_4 remains limited owing to inadequate light absorption capability, swift recombination and low transport efficiency of photogenerated charge carriers [14]. Therefore, considerable efforts have been directed toward facilitating the migration efficiency of photogenerated charge carriers of g-C_3N_4-based photocatalysts by various methods, including elemental doping [13, 15], morphology control [16], cocatalyst loading [17], microstructural regulation [18], and heterostructure construction [19]. Among these strategies, heterostructure construction is commonly considered as an effective approach to boost the separation and migration of photogenerated carriers [20].

Electron transport materials, which are widely utilized in solar cells for selectively transferring electrons [21], have found recent applications in photocatalysis for enhancing the transport of photogenerated electrons. For example, Park's group applied an electron transport layer on $NiCo_2S_4$/CdO photocatalyst to restrain interfacial charge recombination by selectively transporting electrons [22]. However, exploiting electronic transport materials in photocatalysis is still limited by issues such as energy level matching, photo-, thermal- and chemical stability, and high cost. Notably, Tin dioxide (SnO_2) is a wide bandgap (approximately 3.6 eV at 300 K) semiconductor and serves as the electron transport material in solar cells, owing to its chemical stability, outstanding electrical performance, high carrier density, non-toxic and economical cost [23]. Recently, SnO_2 has also been reported to be used in photocatalysis. Byon group advanced the photocatalytic degradation of SnO_2 QDs through Cu doping [24]. Mallikarjuna et al. reported that doping carbon on SnO_2 eventuated in its light absorption edge red shift, thereby improving the photocatalytic H_2 production [25]. Li et al. developed a heterostructure photocatalyst by synthesizing SnO_2 QDs on 2D g-

C_3N_4, which exhibited exceptional styrene epoxidation performance resulting from effective electron transport from g-C_3N_4 to SnO_2 [26]. However, limited studies have concentrated on using SnO_2-based materials as electron transport materials in visible-light-driven H_2 production. Predictably, the selective electron transfer ability of SnO_2-based materials holds promise for promoting the separation and migration of photogenerated charge carriers. Furthermore, constructing SnO_2/g-C_3N_4 heterojunction is still restricted by a series of factors such as limited electron transfer ability, instability of SnO_2 nanostructure, and complex preparation procedure. Barium sulfate ($BaSO_4$) is an insulator material commonly used as a support in the field of catalysis[27]. Due to its remarkable chemical and thermal stability, $BaSO_4$ could effectively disperse and stabilize catalysts in catalytic reactions. Lately, there have also been a few researches exploring its potential photocatalytic applications in combination with semiconductors [28, 29].

In the present work, $SnO_2/BaSO_4$ was synthesized by etching $BaSnO_3$ *via* the wet etching method, a technique commonly used to fabricate nanoparticles with controlled size and morphology [30]. Subsequently, the composite photocatalyst was prepared by combining $SnO_2/BaSO_4$ with g-C_3N_4 using the solvothermal process. $BaSO_4$ could serve as support in the $SnO_2/BaSO_4$ composite, disperse SnO_2 and avoid agglomeration, enabling SnO_2 species to expose more active sites in the photocatalytic H_2 production reaction. The effects of $SnO_2/BaSO_4$ loading on g-C_3N_4 were investigated, including the photocatalytic H_2 production activity, crystallographic structure, morphology, chemical and electronic state, optical characteristics, and photochemical property. Furthermore, the mechanism underlying the amelioration in activity was investigated. We proposed the electron transport channel role of $SnO_2/BaSO_4$ and the mechanism of enhancement of photogenerated carrier separation and migration.

2. Experimental details

2.1. Chemicals

Barium chloride dihydrate ($BaCl_2 \cdot 2H_2O$), tin tetrachloride pentahydrate

($SnCl_4 \cdot 5H_2O$) ethanol (C_2H_5O), urea (CH_4N_2O), ammonia ($NH_3 \cdot H_2O$, 25 wt%), hydrogen peroxide (H_2O_2), citric acid monohydrate ($C_6H_8O_7 \cdot H_2O$), triethanolamine ($C_6H_{15}NO_3$), sodium sulfate (Na_2SO_4), and sulfuric acid (H_2SO_4, 98%) were purchased from Sinopharm Chemical Reagent Co., Ltd. Nafion solution and chloroplatinic acid hexahydrate ($H_2PtCl_6 \cdot 6H_2O$) were sourced from Alfa Aesar. All chemicals were of analytical grade and utilized as obtained without additional processing, and deionized water was employed throughout to prepare the aqueous solutions.

2.2. Synthesis of samples

2.2.1. Synthesis of g-C_3N_4

In a covered 50 mL alumina crucible, urea (20 g) was calcined for 4 h at 550°C with a heating rate of 5°C min^{-1} in a muffle furnace. The product was cooled to room temperature and ground to yield g-C_3N_4 powder, referred to as CN.

2.2.2. Synthesis of $SnO_2/BaSO_4$

The $BaSnO_3$ precursor was synthesized according to the literature method [31]. Specifically, $C_6H_8O_7$ H_2O (5 mmol) was dissolved into H_2O_2 solution (170 mL, 30 wt%) until completely dissolving, followed by the addition of $BaCl_2 \cdot 2H_2O$ (10 mmol) and $SnCl_4 \cdot 5H_2O$ (10 mmol) to the solution. Afterward, $NH_3 \cdot H_2O$ (25 wt%) was added dropwise to the obtained solution until the pH value reached 10, then the solution was kept for 1 h in thermostatic water bath (50°C). Once natural cooled, the acquired suspension was centrifuged, rinsed with deionized water until the pH reached 7, and subsequently dried to acquire the precursor. Then the precursor (1 g) was heated at 550°C for 1 h (5°C min^{-1}) in a muffle furnace, and the obtained $BaSnO_3$ (300 mg) was dispersed into deionized water (167 mL), then sulfuric acid (3 mL, 98%) was slowly added into the suspension under stirring. Next, the beaker was maintained at 35°C for 1 h in a thermostatic water bath. Lastly, the solution underwent centrifugation and drying process to yield $SnO_2/BaSO_4$, which was referred to as SnBaSO.

2.2.3. Synthesis of g-C_3N_4-$SnO_2/BaSO_4$

300 mg of g-C_3N_4 and the required dosage (0, 3, 10, 30, 100, and 300 mg, respectively) of SnBaSO were added to a polytetrafluoroethylene autoclave liner. Then

ethanol (20 mL) was introduced to the mixture followed by 20 min ultrasonication to form a suspension. Afterward, the liner was placed inside an autoclave, which was kept 24 h at 180°C. After natural cooled, the solids were centrifuged, washed with deionized water three times, and dried to acquire a light-yellow powder, CN-SnO_2/$BaSO_4$, which was referred to as CN-*x*SnBaSO (*x* represents 0, 3, 10, 30, 100, and 300, indicating the dosage of SnBaSO).

Characterization, Photocatalytic performance evaluation, and Electrochemical measurement of samples were referred to ***Supplementary Material***.

3. Results and discussion

3.1. Structures

The Powder X-ray diffraction (PXRD) patterns of CN and SnBaSO were displayed in Figure 1a. The characteristic diffraction peaks at 13.2° and 27.3° were indexed to the (100) and (002) planes of g-C_3N_4, corresponding to the interplanar structural packing motif and the interlayer stacking of the conjugated aromatic structures of g-C_3N_4 nanosheets, respectively [32, 33]. As depicted in Figure S1, SnBaSO showed typical characteristic diffraction peaks of $BaSO_4$ (JCPDS#01-089-3749), significantly different from the peaks of $BaSnO_3$ (JCPDS#01-089-2488). However, the peaks of SnO_2 were absent, which was attributed to the amorphous structure of SnO_2 formed under acidic conditions. Furthermore, comparing the peaks between CN and SnBaSO indicated that CN-10SnBaSO, CN-30SnBaSO, CN-100SnBaSO, and CN-300SnBaSO all displayed diffraction peaks of both CN and SnBaSO simultaneously, signifying the successful formation of the composite. Besides, the diffraction peaks of CN gradually weakened while those of SnBaSO became stronger, resulted from the increase of SnBaSO dosage and the inhibitory effect of SnBaSO on the surface structure of CN, namely the guest-host interaction [34, 35].

The Fourier-transform infrared (FTIR) characterization revealed the detail concerning the combination of CN and SnBaSO. As illustrated in Figure 1b and Figure S2, the gradual presence of characteristic bands of SnBaSO was observed, along with an increase in the amount of SnBaSO in the composite. These finding were consistent with the results of PXRD characterization. Additionally, a weak shoulder band of CN-*x*SnBaSO and SnBaSO located at 562 cm^{-1} was ascribed to Sn-O vibration, suggesting SnO_2 species existed in the samples. However, other band assigned to Sn-O vibration (610 and 650 cm^{-1}) coincided with the band of SO_4^{2-}, causing difficulty in distinguishing [36, 37]. The bands at approximately 3500 and 1631 cm^{-1} originated from stretching and bending vibration of O-H in H_2O molecules, respectively. The bands at 610 and 643 cm^{-1} were due to the bending vibration of SO_4^{2-}, whereas those at 983, 1076, 1115 and 1191 cm^{-1} were assigned to the symmetric stretching vibration of SO_4^{2-} [38]. The bands at 1384, 2918 and 2850 cm^{-1} may be due to the organic residue originating from the thermal decomposition of citric acid. Moreover, the bands at 1636, 1570, 1460, 1410, 1324, and 1240 cm^{-1} were ascribed to the stretching vibration of aromatic C-N heterocycles in CN, the broad bands at 3100-3600 cm^{-1} originated from stretching mode of O-H and N-H, the bands at 2920 and 2852 cm^{-1} were assigned to CH_2 and CH_3 vibration in the organic residue originating from the thermal decomposition of citric acid, while the bands at 808 cm^{-1} were assigned to the stretching vibration of the triazine unit in CN [39, 40]. Furthermore, it was noteworthy that CN-*x*SnBaSO showed similar basic characteristic bands to pristine CN, affirming the structural stability of CN during the composite synthesis. The bands attributed to SnO_2 and $BaSO_4$ in the spectra of CN-*x*SnBaSO manifested the successful integration of CN and SnBaSO.

The morphological transition was investigated by scanning electron microscopy (SEM). The stacked curled nanosheet morphology of CN remained mostly unchanged after solvothermal treatment, as evidenced in Figure S3a and b. In contrast, as presented in Figure S3c–g, the morphology of CN-*x*SnBaSO samples evolved from large sheets to smaller ones as the SnBaSO dosage increased. Additionally, Figure S3h depicted SnBaSO samples with numerous particles smaller than 100 nm, corresponding to agglomerated SnBaSO particles. For intuitively revealing the microstructure of CN, CN-0SnBaSO, CN-100SnBaSO, and SnBaSO, transmission electron microscopy (TEM) test was performed. Figure S4a and b demonstrate the typical thin-layer nanosheet morphology of CN. Figure S4c revealed that the size of SnBaSO nanoparticles was approximately 20 nm, similar to the $BaSnO_3$ precursor, confirming the successful synthesis of small-sized SnBaSO particles through $BaSnO_3$ etching. Figure 1c displayed the TEM image of CN-100SnBaSO, showing the presence of SnBaSO nanoparticles on CN nanosheets. Furthermore, high resolution transmission electron microscopy (HRTEM) images of CN-100SnBaSO (Figure 1d and Figure S4d) and energy dispersive spectroscopy (EDS) mapping (Figure S5) further solidified the evidence of SnBaSO nanoparticles loading on CN nanosheets. C, N, Ba, S, Sn, O elements existed in CN-SnBaSO, while Ba, S, Sn, O elements were observed in SnBaSO mapping image. Additionally, Figure S6 showed uniform distribution of Ba, Sn, and O elements, indicating the presence of $BaSnO_3$. Instead, as depicted in Figure S5b, the distributions of Sn and O elements in SnBaSO exhibited significant overlap, and the distributions of Ba and S elements also demonstrated substantial overlap. Conversely, there was less overlap observed between Ba and Sn elements. The same results could also be observed in Figure S5a. In combination with XRD and XPS characterization, this finding substantiated the inference that the primary species in SnBaSO consisted of SnO_2 and $BaSO_4$.

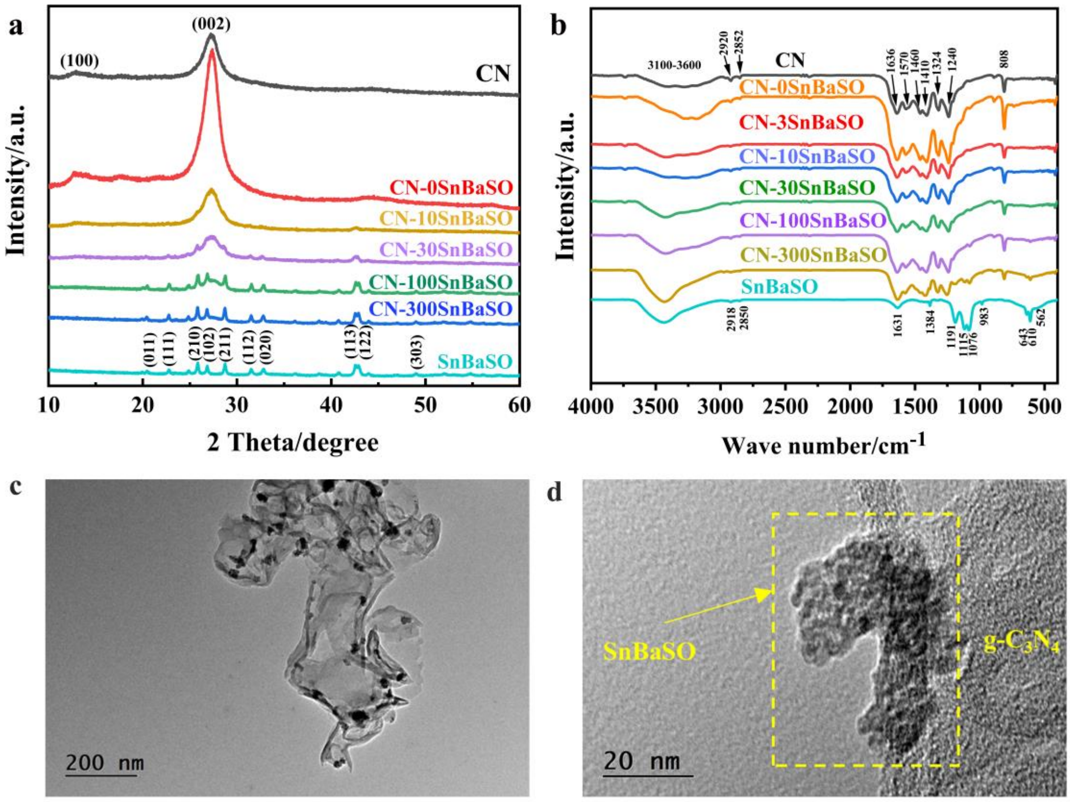

Figure 1. (a) PXRD patterns and (b) FTIR spectra of CN, CN-*x*SnBaSO, and SnBaSO. (c) TEM image of CN-100SnBaSO. (d) HRTEM image of CN-100SnBaSO.

The chemical states of CN-0SnBaSO, CN-100SnBaSO, and SnBaSO were investigated using X-ray photoelectron spectroscopy (XPS). In Figure 2a, CN-100SnBaSO demonstrated Ba, Sn, O, S, N, and C elements. As evidenced in Figure 2b, the O 1s spectrum of CN-0SnBaSO showed characteristic peaks at 533.0 and 531.9 eV, attributed to oxygen in adsorbed water and O-C-N, respectively [41]. The O 1s peaks at 532.2 and 530.9 eV were assigned to SO_4^{2-} and Sn-O for SnBaSO, respectively [42]. Similarly, in the O 1s spectrum of CN-100SnBaSO, the peaks at 532.9 and 531.1 eV were assigned to oxygen in adsorbed water and Sn-O, respectively. The peak at 532.1 eV was attributed to SO_4^{2-} or O-C-N. Ba 3d spectrum of CN-100SnBaSO (Figure 2c) revealed that the spacing between the two split peaks was 15.2 eV. Compared to Ba 3d peaks of $BaSnO_3$, the Ba 3d peaks of SnBaSO shifted to higher binding energy, which was due to the changes in chemical environment caused by coordination of Ba with S. Comparative analysis of the Ba 3d peaks between CN-100SnBaSO and SnBaSO revealed that binding energy shift to a higher energy, indicative of an electron-deficient chemical environment for Ba. This result originated from charge redistribution induced by the coordination of Ba with the electronegative C and N species in CN. Furthermore, the Sn 3d spectrum of the SnBaSO sample displayed peaks at 487.0 and 495.4 eV, assigned to Sn 3$d_{5/2}$ and Sn 3$d_{3/2}$, respectively, indicating Sn existed in the form of Sn^{4+} [43]. Compared to Sn 3d peaks of $BaSnO_3$, the Sn 3d peaks of SnBaSO shifted to higher binding energy, which also illustrated the changes in the chemical environment. It was noteworthy that after being combined with CN, the Sn 3d peaks of SnBaSO shifted to a lower binding energy of 0.3 eV, and similar results were observed in the corresponding O 1s peaks of Sn-O, which shifted to a lower binding energy of 0.2 eV, as shown in Figure 2d and Table S1. These results illustrated the electrons on CN tended to migrate to SnO_2, which led to the enrichment of electrons of SnO_2, suggesting SnBaSO became a new electron transport channel on CN.

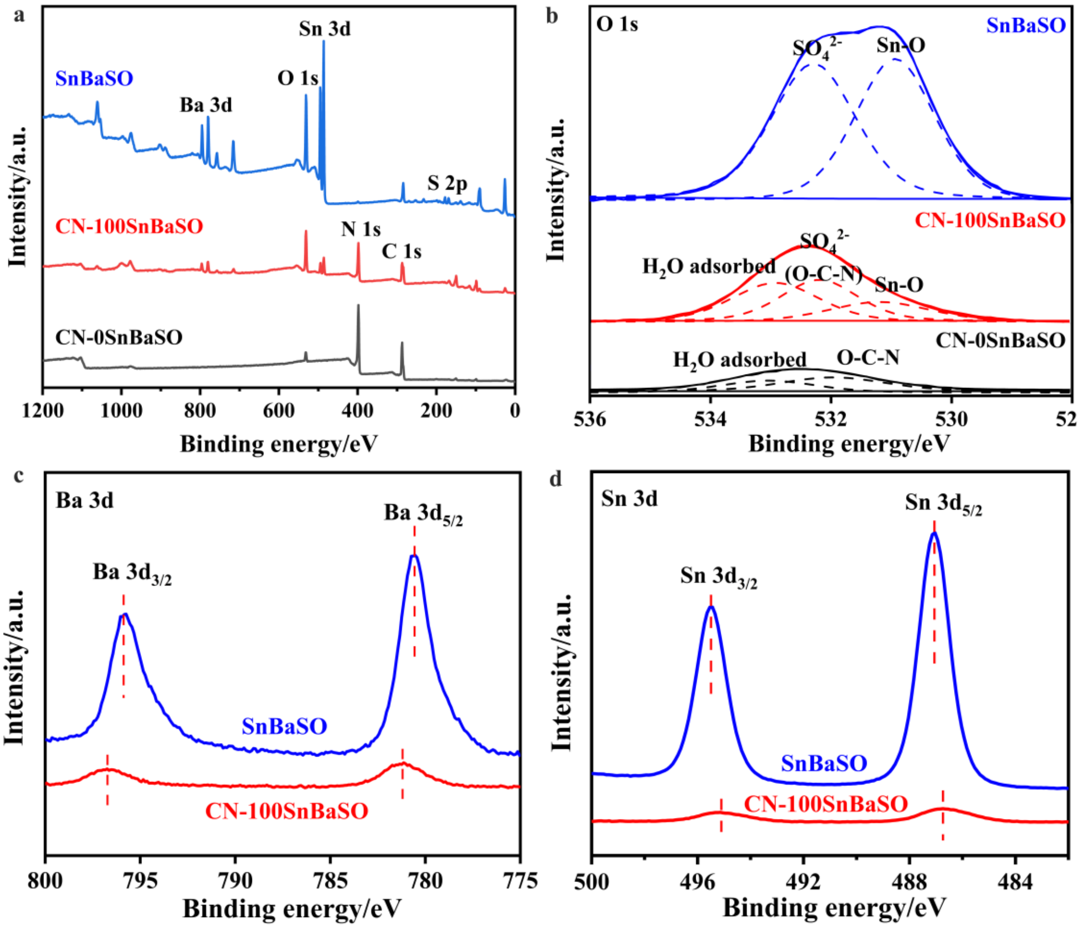

Figure 2. (a) XPS survey spectra of CN-0SnBaSO, CN-100SnBaSO, and SnBaSO. (b) High-resolution O 1s XPS spectra of CN-0SnBaSO, CN-100SnBaSO, and SnBaSO. (c)

High-resolution Ba 3d XPS spectra of CN-100SnBaSO and SnBaSO. (d) High-resolution Sn 3d XPS spectra of CN-100SnBaSO and SnBaSO.

Nitrogen adsorption and desorption curves exhibited a small amount of adsorption at low pressure and a significant increase as pressure increased (Figure S8a), while the hysteresis loop was not apparent, suggesting the presence of fewer micro- and mesopores. The specific surface areas of CN, CN-0SnBaSO, CN-100SnBaSO, and SnBaSO were 50.7, 53.2, 59.3, and 85.0 m^2 g^{-1}, respectively. The SnBaSO introduction resulted in a slight increase in the specific surface area. As displayed in Figure S8b, the CN-0SnBaSO and CN-100SnBaSO samples possessed more pores of approximately 20 nm, which was due to the increased fragmentation of the nanosheets resulting from the solvothermal treatment of CN. It was noteworthy that the pore structures of CN-0SnBaSO and CN-100SnBaSO were analogous, suggesting that the porous structure was unaffected by the addition of SnBaSO.

Thermogravimetry Analysis (TGA) results in Figure S9a and b showed that CN and CN-0SnBaSO left no residue after treatment at 800°C because CN converted into gaseous products completely. There was little change in SnBaSO quality after being treated at 800°C, while the weight loss curve of CN-100SnBaSO exhibited partial weight residue, attributed to the SnBaSO component. As presented in Figure S9b, two exothermic peaks were noticed in the differential scanning calorimetry (DSC) curves of CN-100SnBaSO during the heating process, which might be due to the fact that the introduction of SnBaSO advanced the decomposition temperature of a portion of CN nanosheets.

3.2. Light absorption and photogenerated carrier dynamics

Ultraviolet–visible (UV–vis) spectra of CN, CN-*x*SnBaSO, $BaSnO_3$ and SnBaSO were recorded to investigate the light absorption. As present in Figure 3a, the absorption edge of CN and $BaSnO_3$ was approximately 450 nm and 400 nm, respectively, consistent with previously reported results [44, 45]. The spectrum of SnBaSO showed a significant blue shift compared to $BaSnO_3$, and the absorption edge of SnBaSO was approximately 325 nm, which could hardly utilize visible light. However, the band gap of CN was almost unaffected by the addition of SnBaSO. Furthermore, as depicted in Figure S10a, $BaSO_4$ exhibited no absorption of light, thus the light absorption of SnBaSO materials originated from SnO_2. The Mott-Schottky (M-S) tests were conducted to obtain information on the band structure of CN and SnBaSO. As evidenced in Figure S11, the slope of the longest linear part of the curves of CN and SnO_2 were both positive, corresponding to n-type semiconductors. The flat band potential of CN and SnO_2 was estimated to be −1.31 V vs. RHE and −1.11 V vs. RHE, respectively. Accordingly, the conduction band (CB) potential of CN and SnO_2 was estimated to be −1.51 and −1.31 eV, respectively. Combined with the band gap of CN and SnO_2 (2.88 and 4.10 eV, respectively) obtained by the Tauc-plot (Figure S10b), the band structure was illustrated in Figure 3b. According to the above results, it could be deduced that the photogenerated electron on CN transformed to the CB of SnO_2.

The charge transfer properties were offered by the electrochemical impedance spectra (EIS) test, as illustrated by the Nyquist plots in Figure 3c. The smaller arc radius of CN-100SnBaSO demonstrated reduced charge transfer resistance, corresponding to faster photogenerated carriers transfer, as well as increased availability of carriers for the reaction. The transient photocurrent response test (Figure 3d) obviously revealed that CN-100SnBaSO exhibited the strongest photocurrent response intensity. This result confirmed the highly efficient separation ability of photoinduced charges for CN-100SnBaSO, which was consistent with the EIS results. Moreover, the steady-state photoluminescence (PL) spectra were recorded to reflect the photogenerated carrier recombination behavior of photocatalysts, as shown in Figure 3e. Compared with CN and CN-0SnBaSO, the fluorescence intensity of CN-100SnBaSO was significantly quenched, suggesting the photogenerated electron-hole pairs were effectively separated and the recombination was inhibited owing to the electron transport function of SnBaSO. As illustrated in Figure 3f, the time-resolved photoluminescence spectra were obtained to further investigate the charge transfer dynamics. The average fluorescence lifetime of CN-100SnBaSO (2.50 ns) was longer than that of CN (2.20 ns) and CN-0SnBaSO (1.77 ns), confirming enhanced photogenerated charge transfer and inhibition of recombination on CN-100SnBaSO. The above analyses suggested SnBaSO material served as an electron transport channel in the photocatalyst.

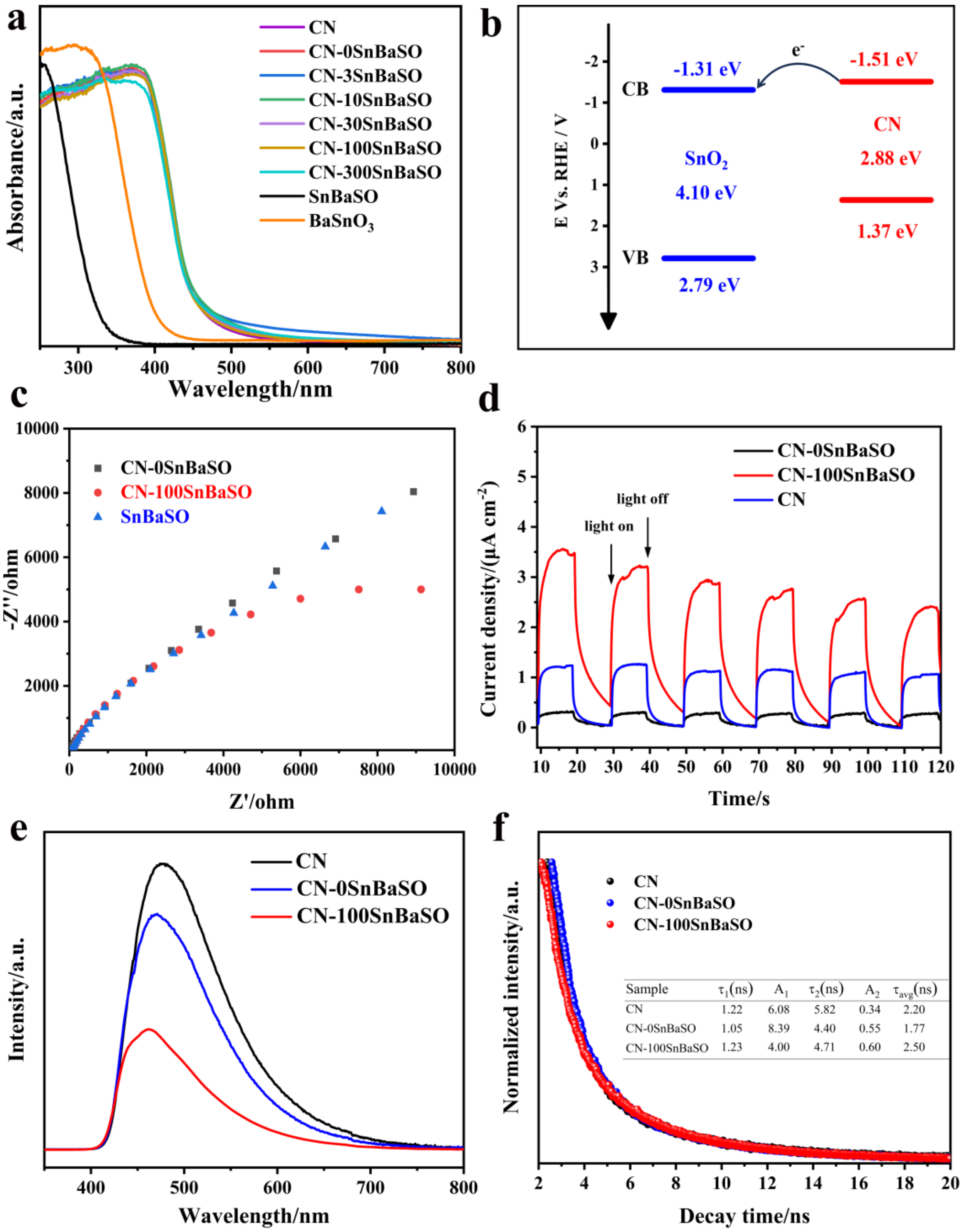

Sample	τ_1(ns)	A_1	τ_2(ns)	A_2	τ_{avg}(ns)
CN	1.22	6.08	5.82	0.34	2.20
CN-0SnBaSO	1.05	8.39	4.40	0.55	1.77
CN-100SnBaSO	1.23	4.00	4.71	0.60	2.50

Figure 3. (a) UV–vis spectra of CN, SnBaSO, $BaSnO_3$ and CN-*x*SnBaSO. (b) Energy bands of CN and SnO_2. (c) EIS Nyquist plots of CN-0SnBaSO, CN-100SnBaSO, and SnBaSO. (d) Photocurrent density of CN, CN-0SnBaSO and CN-100SnBaSO. (e) Steady state PL spectra and (f) Time-resolved PL spectra of CN, CN-0SnBaSO and CN-100SnBaSO at room temperature.

3.3. Photocatalytic H_2 production activity and mechanism

The photocatalytic H_2 production activities of CN and CN-xSnBaSO samples under visible light were presented in Figure 4a. The comparison between the activities of CN and CN-0SnBaSO revealed that the solvothermal treatment had little effect on the activity of CN. Furthermore, the activity of CN-xSnBaSO exhibited an initial increase followed by a subsequent decrease as the SnBaSO dosage was increased. Notably, CN-100SnBaSO exhibited the highest activity of 14.2 μmol h^{-1}, which was 2.5 and 2.8 times higher than that of CN (6.1 μmol h^{-1}) and CN-0SnBaSO (5.3 μmol h^{-1}), respectively (Figure 4b). The apparent quantum efficiency (AQE) of photocatalytic H_2 production was calculated to be 3.4% at 420 nm. Figure 4c displayed that the activity of CN-100SnBaSO remained stable for two cycles but experienced a 15% decrease in the third cycle. This decline might be due to the partial detachment of SnBaSO after the photocatalyst was immersed in the solution overnight.

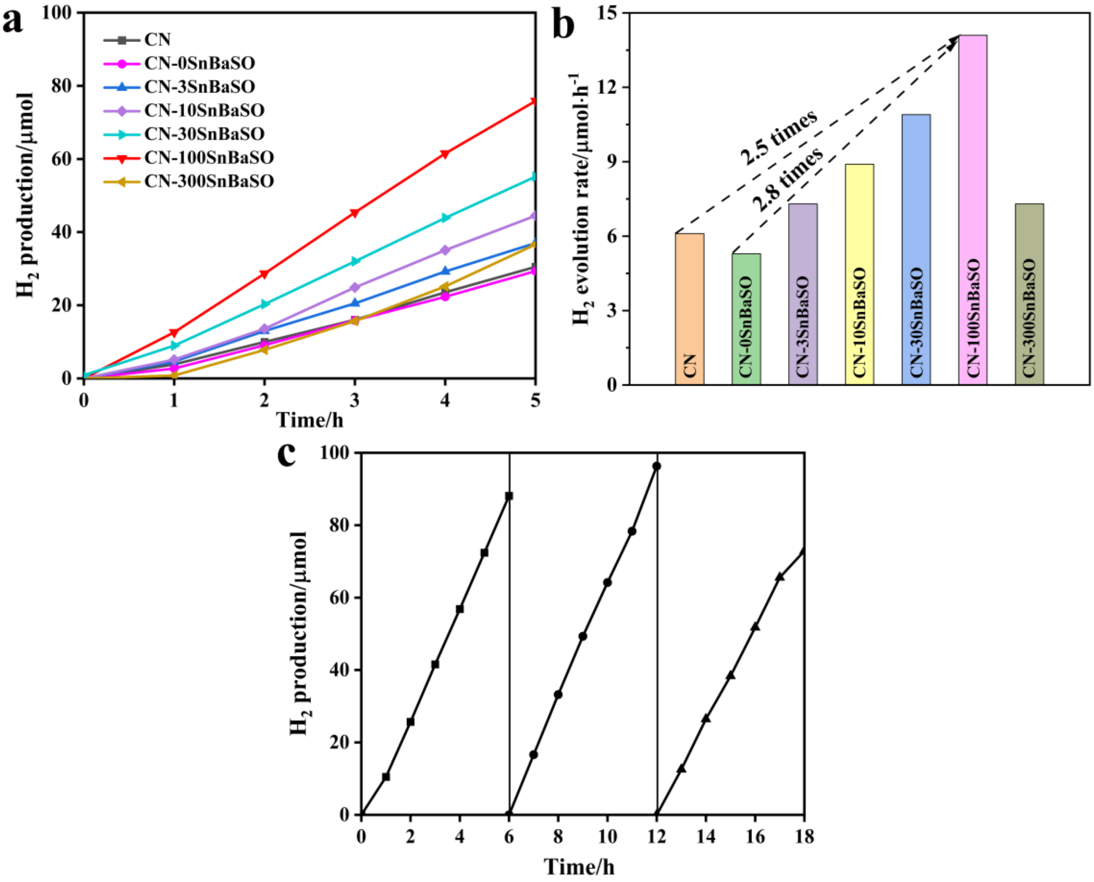

Figure 4. (a) Photocatalytic H_2 production activities of CN and CN-xSnBaSO. (b) Average photocatalytic H_2 production rate of CN and CN-xSnBaSO. (c) Photocatalyst

stability test of CN-100SnBaSO.

To verify the role of $BaSO_4$ in the SnBaSO, we synthesized SnO_2 in similar procedure without adding $BaCl_2·2H_2O$ and then prepared CN-SnO_2 using solvothermal method under the same condition as CN-*x*SnBaSO. As shown in Figure S12, the photocatalytic H_2 production rate of CN-SnO_2 was lower than that of CN-100SnBaSO, the similar trend was also reflected in the photocurrent density of CN-SnO_2 and CN-100SnBaSO (Figure S13). In addition, Figure S14 demonstrated the lower fluorescence intensity and the longer average fluorescence lifetime of CN-100SnBaSO. The above results indicated the better photogenerated charge transport ability of CN-100SnBaSO, and validated that $BaSO_4$ affected the photogenerated charge transport.

Based on the structural characterization, the energy band structure analysis and photogenerated carrier dynamics investigation of the photocatalyst, it could be demonstrated that SnBaSO effectively integrated with CN, establishing an electron transport channel on CN. Consequently, this integration promoted the transport of photogenerated electrons, enhancing the photocatalytic H_2 production activity. To further confirm the electron transport role of SnBaSO loaded on CN and the formation of type II heterojunction, a charge transfer tracking experiment was conducted by selective photo-deposition of the noble metal Pt using H_2PtCl_6 as a precursor. TEM images and EDS mapping of Pt-loaded CN-100SnBaSO were obtained. As shown in Figure 5a, CN nanosheets, SnBaSO nanoparticles, and Pt nanoparticles were observed in the TEM image. Figure 5b and c showed the presence of photo-deposited Pt nanoparticles on both CN and SnBaSO, but with a significantly greater inclination towards deposition on SnBaSO. Moreover, the elemental distribution shown in Figure 5d manifested the Pt element overlapped more with Ba, S, Sn and O elements, confirming that Pt atoms were more likely to be deposited on SnBaSO. Since the Pt co-catalyst employed in this research was derived from $H_2PtCl_6·H_2O$ *via* a photo-deposition reduction reaction, the preference of Pt to be deposited on SnBaSO indicated that SnBaSO provided a reduction environment, which demonstrated that the photogenerated electrons mainly accumulated on SnBaSO. This results further validated that SnBaSO loading on CN acted as an electron channel, and the photogenerated electrons on CN excitation by visible light transferred to SnBaSO. The combination of TEM and corresponding EDS mapping images with aforementioned band structure analysis demonstrated the formation of type II heterojunction between CN and SnO_2.

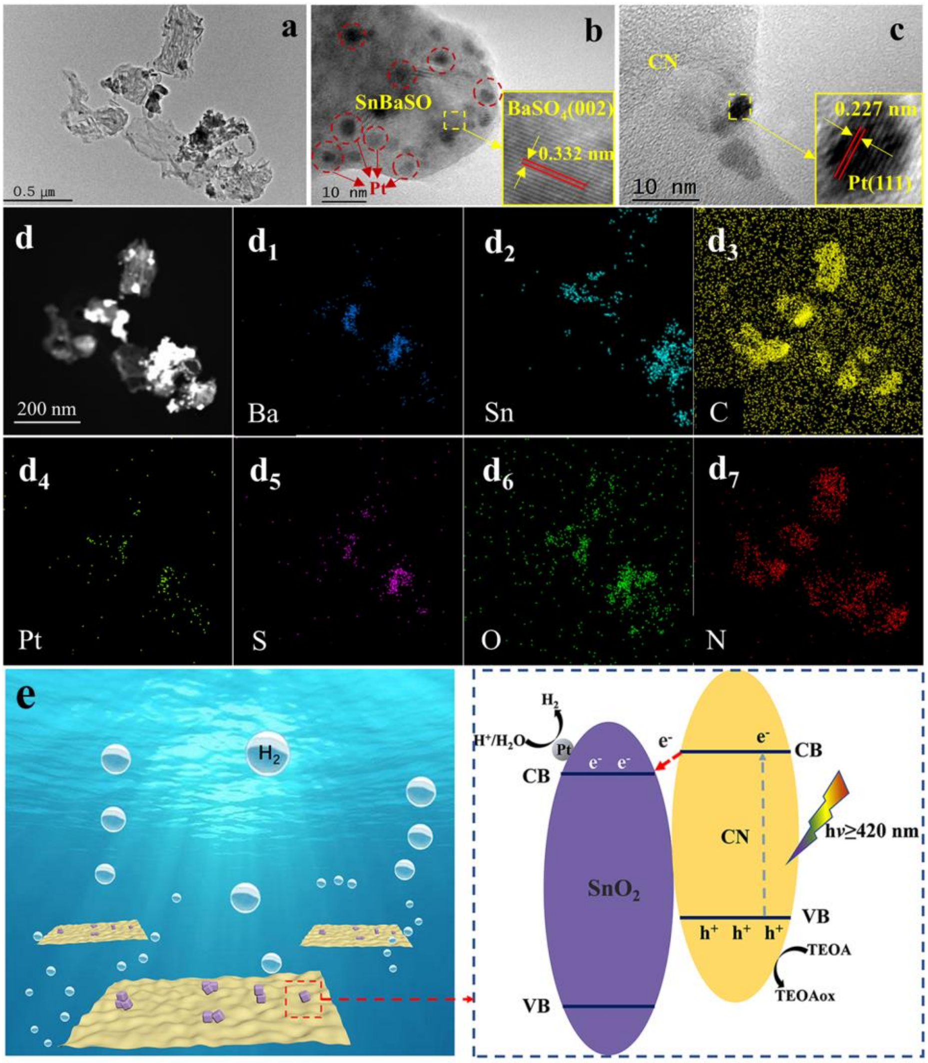

Figure 5. (a) TEM image, (b, c) HRTEM images, and (d) EDS mapping images of Pt-loaded CN-100SnBaSO. (e) Schematic diagram of the visible-light-driven photocatalytic H_2 production mechanism of the photocatalyst.

The photocatalytic mechanism of the CN-100SnBaSO photocatalyst could be speculated according to the analysis presented, which was illustrated in Figure 5e. Heterojunction was formed through the successful loading of SnBaSO on CN nanosheets *via* the solvothermal process. The photogenerated electrons on CN rapidly transferred to SnBaSO nanoparticles upon excitation by visible light. These photogenerated electrons then participated in the H_2 production, while the photogenerated holes were depleted by the hole scavenger TEOA molecules. SnBaSO nanoparticles played an essential role as the electron transport channel in facilitating the photogenerated electrons transport, thereby accelerating the reaction. Furthermore, it is essential to note that the spatial separation of photogenerated charge carriers contributed to preventing recombination, which was imperative for maintaining the catalytic activity of the photocatalyst.

4. Conclusion

In summary, the $SnO_2/BaSO_4$ nanoparticles were synthesized using wet etching method, and the CN-$SnO_2/BaSO_4$ photocatalyst for photocatalytic H_2 production was subsequently fabricated by incorporating g-C_3N_4 and $SnO_2/BaSO_4$ through solvothermal treatment. The successful synthesis of the CN-$SnO_2/BaSO_4$ improved the photocatalytic H_2 production performance. Specifically, the CN-100SnBaSO photocatalyst demonstrated the highest H_2 production performance of 14.2 μmol h^{-1} under visible light, which was 2.5 times higher than that of pristine g-C_3N_4. The enhanced performance could be credited to the $SnO_2/BaSO_4$ nanoparticles on g-C_3N_4, which functioned as an electron transport channel, thereby facilitating the migration of photogenerated carriers.

Acknowledgments

This work is supported by the National Key Research and Development Program of China (No. 2022YFB3803600), the National Natural Science Foundation of China (No. 52206276), the China Postdoctoral Science Foundation (No. 2022M712517), the Key Research and Development Program of Shaanxi Province (No. 2024GX-YBXM-459), and the Fundamental Research Funds for the Central Universities. We appreciate Dr. Jiamei Liu from Instrumental Analysis Center of Xi'an Jiaotong University for the structural analysis.

References

[1] M. Rastgar, K. Moradi, C. Burroughs, A. Hemmati, E. Hoek, M. Sadrzadeh, Harvesting Blue Energy Based on Salinity and Temperature Gradient: Challenges, Solutions, and Opportunities, Chem. Rev. 123 (16) (2023) 10156-10205.

[2] R. Way, M.C. Ives, P. Mealy, J.D. Farmer, Empirically grounded technology forecasts and the energy transition, Joule 6 (9) (2022) 2057-2082.

[3] A. Odenweller, F. Ueckerdt, G.F. Nemet, M. Jensterle, G. Luderer, Probabilistic feasibility space of scaling up green hydrogen supply, Nature Energy 7 (9) (2022) 854-865.

[4] S. Wei, R. Sacchi, A. Tukker, S. Suh, B. Steubing, Future environmental impacts of global hydrogen production, Energy & Environmental Science 17 (6) (2024) 2157-2172.

[5] P. Jiménez-Calvo, Synergy of visible-light responsive photocatalytic materials and device engineering for energy and environment: Minireview on hydrogen production and water decontamination, Materials Today Catalysis 4 (2024) 100040.

[6] J. Kosco, S. Gonzalez-Carrero, C.T. Howells, T. Fei, Y. Dong, R. Sougrat, G.T. Harrison, Y. Firdaus, R. Sheelamanthula, B. Purushothaman, F. Moruzzi, W. Xu, L. Zhao, A. Basu, S. De Wolf, T.D. Anthopoulos, J.R. Durrant, I. McCulloch, Generation of long-lived charges in organic semiconductor heterojunction nanoparticles for efficient photocatalytic hydrogen evolution, Nature Energy 7 (4) (2022) 340-351.

[7] C. Cheng, J. Shi, L. Mao, C.-L. Dong, Y.-C. Huang, S. Zong, J. Liu, S. Shen, L. Guo, Ultrathin porous graphitic carbon nitride from recrystallized precursor toward significantly enhanced photocatalytic water splitting, J. Colloid Interface Sci. 637 (2023) 271-282.

[8] J. Di, W. Jiang, Recent progress of low-dimensional metal sulfides photocatalysts for energy and environmental applications, Materials Today Catalysis 1 (2023) 100001.

[9] J. Fan, H. Wang, W. Sun, H. Duan, J. Jiang, Recent developments and perspectives of Ti-based transition metal carbides/nitrides for photocatalytic applications: A critical review, Mater. Today 76 (2024) 110-135.

[10] X. Wang, K. Maeda, A. Thomas, K. Takanabe, G. Xin, J.M. Carlsson, K. Domen, M. Antonietti, A metal-free polymeric photocatalyst for hydrogen production from water under visible light, Nat. Mater. 8 (1) (2009) 76-80.

[11] S.R. Nagella, R. Vijitha, B. Ramesh Naidu, K.S.V. Krishna Rao, C.-S. Ha, K. Venkateswarlu, Benchmarking recent advances in hydrogen production using g-C_3N_4-based photocatalysts, Nano Energy 111 (2023) 108402.

[12] C. Cheng, L. Mao, X. Kang, C.-L. Dong, Y.-C. Huang, S. Shen, J. Shi, L. Guo, A high-cyano groups-content amorphous-crystalline carbon nitride isotype heterojunction photocatalyst for high-quantum-yield H_2 production and enhanced CO_2 reduction, Applied Catalysis B: Environmental 331 (2023) 122733.

[13] Y. Chen, B. Zhang, Y. Liu, J. Chen, H. Pan, W. Sun, Graphitic carbon nitride-based electrocatalysts for energy applications, Materials Today Catalysis 1 (2023) 100003.

[14] L. Mao, B. Zhai, L. Wen, W. Xiao, J. Shi, X. Kang, Y. Liu, C. Cheng, H. Jin, L. Guo, Simultaneous bulk and surface modifications of g-C_3N_4 via supercritical CO_2-assisted post-treatment towards enhanced photocatalytic activity, Applied Catalysis B: Environment and Energy 362 (2025) 124712.

[15] H. Wang, J. Jiang, L. Yu, J. Peng, Z. Song, Z. Xiong, N. Li, K. Xiang, J. Zou, J.-P. Hsu, T. Zhai, Tailoring Advanced N-Defective and S-Doped g-C_3N_4 for Photocatalytic H_2 Evolution, Small 19 (28)

(2023) 2301116.

[16] K. Zhang, L. Wang, X. Sheng, M. Ma, M.S. Jung, W. Kim, H. Lee, J.H. Park, Tunable Bandgap Energy and Promotion of H_2O_2 Oxidation for Overall Water Splitting from Carbon Nitride Nanowire Bundles, Advanced Energy Materials 6 (11) (2016) 1502352.

[17] K. Wang, S. Yang, Y. Wu, Enhanced photocatalytic water splitting of g-C_3N_4 loaded with Fe doped Co_3O_4 and Pt dual-cocatalysts, Journal of Environmental Chemical Engineering 10 (5) (2022) 108353.

[18] M. Ren, X. Zhang, Y. Liu, G. Yang, L. Qin, J. Meng, Y. Guo, Y. Yang, Interlayer Palladium-Single-Atom-Coordinated Cyano-Group-Rich Graphitic Carbon Nitride for Enhanced Photocatalytic Hydrogen Production Performance, ACS Catalysis 12 (9) (2022) 5077-5093.

[19] S.-Z. Zhao, R. Lu, Y. Yang, Y. Lu, R.D. Rodriguez, J.-J. Chen, Direct Z-scheme g-C_3N_4/TiO_2 heterojunction porous nanotubes: An ingenious synthesis strategy to enhance photocatalytic activity, Journal of Environmental Chemical Engineering 11 (2) (2023) 109366.

[20] L. Xu, B. Tian, T. Wang, Y. Yu, Y. Wu, J. Cui, Z. Cao, J. Wu, W. Zhang, Q. Zhang, J. Liu, Z. Li, Y. Tian, Direct Z-scheme polymeric heterojunction boosts photocatalytic hydrogen production via a rebuilt extended π-delocalized network, Energy & Environmental Science 15 (12) (2022) 5059-5068.

[21] J. Cao, B. Wu, R. Chen, Y. Wu, Y. Hui, B.-W. Mao, N. Zheng, Efficient, Hysteresis-Free, and Stable Perovskite Solar Cells with ZnO as Electron-Transport Layer: Effect of Surface Passivation, Adv. Mater. 30 (11) (2018) 1705596.

[22] H. Anwer, H. Lee, H.-R. Kim, H.-K. Kim, J.-W. Park, Selective transport and separation of charge–carriers by an electron transport layer in $NiCo_2S_4$/CdO@CC for excellent water splitting, Applied Catalysis B: Environmental 265 (2020) 118564.

[23] S.Y. Park, K. Zhu, Advances in SnO_2 for Efficient and Stable n–i–p Perovskite Solar Cells, Adv. Mater. 34 (27) (2022) 2110438.

[24] B. Babu, A.N. Kadam, R.V.S.S.N. Ravikumar, C. Byon, Enhanced visible light photocatalytic activity of Cu-doped SnO_2 quantum dots by solution combustion synthesis, J. Alloys Compd. 703 (2017) 330-336.

[25] K. Mallikarjuna, G.A.K.M. Rafiqul Bari, S.V.P. Vattikuti, H. Kim, Synthesis of carbon-doped SnO_2 nanostructures for visible-light-driven photocatalytic hydrogen production from water splitting, Int. J. Hydrogen Energy 45 (57) (2020) 32789-32796.

[26] M. Li, L. Ma, L. Luo, Y. Liu, M. Xu, H. Zhou, Y. Wang, Z. Li, X. Kong, H. Duan, Efficient photocatalytic epoxidation of styrene over a quantum-sized SnO_2 on carbon nitride as a heterostructured catalyst, Applied Catalysis B: Environmental 309 (2022) 121268.

[27] C. Tian, S.-H. Chai, D.R. Mullins, X. Zhu, A. Binder, Y. Guo, S. Dai, Heterostructured $BaSO_4$–SiO_2 mesoporous materials as new supports for gold nanoparticles in low-temperature CO oxidation, Chem. Commun. 49 (33) (2013) 3464-3466.

[28] W. Cui, L. Chen, J. Li, Y. Zhou, Y. Sun, G. Jiang, S.C. Lee, F. Dong, Ba-vacancy induces semiconductor-like photocatalysis on insulator $BaSO_4$, Applied Catalysis B: Environmental 253 (2019) 293-299.

[29] Q. Chen, H. Zhou, J. Wang, J. Bi, F. Dong, Activating earth-abundant insulator $BaSO_4$ for visible-light induced degradation of tetracycline, Applied Catalysis B: Environment and Energy 307 (2022) 121182.

[30] M. Sun, J. Tian, Q. Chen, The studies on wet chemical etching via in situ liquid cell TEM, Ultramicroscopy 231 (2021) 113271.

[31] S.S. Shin, E.J. Yeom, W.S. Yang, S. Hur, M.G. Kim, J. Im, J. Seo, J.H. Noh, S.I. Seok, Colloidally

prepared La-doped $BaSnO_3$ electrodes for efficient, photostable perovskite solar cells, Science 356 (6334) (2017) 167-171.

[32] Z.-F. Huang, J. Song, L. Pan, Z. Wang, X. Zhang, J.-J. Zou, W. Mi, X. Zhang, L. Wang, Carbon nitride with simultaneous porous network and O-doping for efficient solar-energy-driven hydrogen evolution, Nano Energy 12 (2015) 646-656.

[33] X. Chen, H. Chen, J. Guan, J. Zhen, Z. Sun, P. Du, Y. Lu, S. Yang, A facile mechanochemical route to a covalently bonded graphitic carbon nitride (g-C_3N_4) and fullerene hybrid toward enhanced visible light photocatalytic hydrogen production, Nanoscale 9 (17) (2017) 5615-5623.

[34] J. Zhang, G. Zhang, J. Zhang, Organic/inorganic nitride heterostructure for efficient photocatalytic oxygen evolution, Appl. Surf. Sci. 475 (2019) 256-263.

[35] X. She, J. Wu, H. Xu, J. Zhong, Y. Wang, Y. Song, K. Nie, Y. Liu, Y. Yang, M.-T.F. Rodrigues, R. Vajtai, J. Lou, D. Du, H. Li, P.M. Ajayan, High Efficiency Photocatalytic Water Splitting Using 2D α-Fe_2O_3/g-C_3N_4 Z-Scheme Catalysts, Advanced Energy Materials 7 (17) (2017) 1700025.

[36] M. Aziz, S. Saber Abbas, W.R. Wan Baharom, Size-controlled synthesis of SnO_2 nanoparticles by sol–gel method, Mater. Lett. 91 (2013) 31-34.

[37] R. Scipioni, D. Gazzoli, F. Teocoli, O. Palumbo, A. Paolone, N. Ibris, S. Brutti, M.A. Navarra, Preparation and Characterization of Nanocomposite Polymer Membranes Containing Functionalized SnO_2 Additives, Membranes 4 (1) (2014) 123-142.

[38] S.S.J. Dhas, S. Suresh, A. Rita, S.A.M.B. Dhas, R. Gowri Shankar Rao, C.S. Biju, Effect of annealing on the photoluminescence and thermoluminescence properties of Eu^{2+} doped $BaSO_4$ microgravels, J. Mater. Sci.: Mater. Electron. 31 (14) (2020) 11113-11122.

[39] L. Zhang, Z. Jin, Y. Li, X. Hao, F. Han, Zn–Ni–P Nanoparticles Decorated g-C_3N_4 Nanosheets Applicated as Photoanode in Photovoltaic Fuel Cells, Catal. Lett. 149 (9) (2019) 2397-2407.

[40] L. Xia, Z. Sun, Y. Wu, X.-F. Yu, J. Cheng, K. Zhang, S. Sarina, H.-Y. Zhu, H. Weerathunga, L. Zhang, J. Xia, J. Yu, X. Yang, Leveraging doping and defect engineering to modulate exciton dissociation in graphitic carbon nitride for photocatalytic elimination of marine oil spill, Chem. Eng. J. 439 (2022) 135668.

[41] H. Liu, D. Chen, Z. Wang, H. Jing, R. Zhang, Microwave-assisted molten-salt rapid synthesis of isotype triazine-/heptazine based g-C_3N_4 heterojunctions with highly enhanced photocatalytic hydrogen evolution performance, Applied Catalysis B: Environmental 203 (2017) 300-313.

[42] R. Tian, Y. Zhang, Z. Chen, H. Duan, B. Xu, Y. Guo, H. Kang, H. Li, H. Liu, The effect of annealing on a 3D SnO_2/graphene foam as an advanced lithium-ion battery anode, Scientific Reports 6 (1) (2016) 19195.

[43] K. Jung, D.H. Kim, J. Kim, S. Ko, J.W. Choi, K.C. Kim, S.-G. Lee, M.-J. Lee, Influence of a UV-ozone treatment on amorphous SnO_2 electron selective layers for highly efficient planar $MAPbI_3$ perovskite solar cells, Journal of Materials Science & Technology 59 (2020) 195-202.

[44] Q. Wu, S. Zhang, S. Li, Y. Yan, S. Yu, R. Zhao, L. Huang, Chitosan-based carbon dots with multi-color-emissive tunable fluorescence and visible light catalytic enhancement properties, Nano Res. 16 (2) (2023) 1835-1845.

[45] X. Wang, B. Leng, Q. Ren, Z. Yang, J. Xin, X. Wang, Formation and dissociation of excitons in La^{3+}-doped $BaSnO_3$ and improvement of ethanol sensitivity: Heating, nano-$CdSnO_3$ decoration and UV illumination, J. Alloys Compd. 926 (2022) 166812.